Layered crustal anisotropy around the San Andreas Fault near Parkfield, California

Pascal Audet

Department of Earth Sciences, University of Ottawa, Canada

P. Audet, Department of Earth Sciences, University of Ottawa, 120 University, Ottawa, ON, K1N 6N5, Canada. (pascal.audet@uottawa.ca)

Abstract. The rheology of the Earth's crust controls the long-term and short-term strength and stability of plate boundary faults, and depends on the architecture and physical properties of crustal materials. In this paper we examine the seismic structure and anisotropy of the crust around the San Andreas Fault (SAF) near Parkfield, California, using teleseismic receiver functions. These data indicate that the crust is characterized by spatially variable and strongly anisotropic upper and mid crustal layers, with a Moho at $\sim$35 km depth. The upper layer is $\sim$5-10 km thick and is characterized by strong ($\geq$30%) anisotropy with a slow axis of hexagonal symmetry, where the plane of fast velocity has a strike parallel to that of the SAF and a dip of $\sim$40°. We interpret this layer as pervasive fluid-filled microcracks within the brittle deformation regime. The $\sim$10-15 km-thick mid crustal layer is also characterized by a weak axis of hexagonal symmetry with $\geq$20% anisotropy, but the dip-direction of the plane of fast velocity is reversed. The mid crustal anisotropic layer is more prominent to the north-east of the San Andreas Fault. We interpret the mid crustal anisotropic layer as fossilized fabric within fluid-rich foliated mica schists. When combined with various other geophysical observations, our results suggest that fault creep behavior around Parkfield is favored by intrinsically weak and overpressured crustal fabric.

1. Introduction

Synoptic models of depth-dependent rheology at plate boundary fault zones are commonly used to understand the distribution of earthquakes in the Earth's crust [*Handy and Brun*, 2004]. In these models, faults slip seismically along sharp slip planes in the upper, brittle portion of the crust and by steady, aseismic creep on widely distributed shear zones below [e.g., *Handy et al.*, 2007]. These models usually fail to explain the seismicity and strength of the central San Andreas Fault near Parkfield, California, where they vary laterally along strike and with depth. To the southeast of Parkfield, the fault is locked and typically slips in large magnitude earthquakes; to the northwest, the fault creeps at a rate as high as 28 mm yr^{-1} [*Titus et al.*, 2006]. In the creeping section the fault has been interpreted to slip at a shear stress considerably lower than that expected for typical rock and fault gouge friction coefficients, as evidenced by a lack of thermal anomaly from frictional heating [*Lachenbruch and Hass*, 1980; *Sass et al.*, 1997; *Fulton et al.*, 2004] and maximum principal compressive stress oriented almost normal to the fault [*Zoback et al.*, 1987; *Townend and Zoback*, 2004], implying that the fault is weak in an absolute sense. Within the brittle crust, possible causes of a weak fault include, among others, the presence of frictionally weak minerals [e.g., *Moore and Rymer*, 2007] and supra-hydrostatic fluid pressure [e.g., *Hardebeck and Hauksson*, 1999]. The lateral transition between the creeping and locked segments is characterized by the regular occurrence of magnitude M$\sim$6 earthquakes, as well as the occurrence of deep tremors and low-frequency earthquakes (also referred to as slow earthquakes) at middle to lower crustal depth [*Nadeau and Dolenc*, 2005; *Shelly and Hardebeck*, 2010].

These slow earthquakes exhibit properties that are particularly important in refining rheological models of the San Andreas Fault. They generally occur adjacent to, and deeper than, the seismogenic part of the fault [*Schwartz and Rokosky*, 2007; *Beroza and Ide*, 2011], they are 1000 to 10,000 times more sensitive to external forcings [*Rubinstein et al.*, 2007a, b; *Peng et al.*, 2008; *Thomas et al.*, 2009] and range in character from slow aseismic to fast seismic slip [*Peng and Gomberg*, 2010]. Although slow earthquakes were discovered in young and warm circum-Pacific subduction zones, they are now found in a variety of geologic environments where pressure and temperature conditions are vastly different. Proposed mechanisms for slow earthquake slip revolve around the transition between stable and unstable frictional sliding caused by low effective normal stress, controlled in part by the presence of fluid overpressures [*Johnson et al.*, 2013]. Evidence for a weak and overpressured fault at lower crustal depth include the modulation of tremor activity by solid Earth tides [*Rubinstein et al.*, 2007a; *Thomas et al.*, 2009], tremor triggering by passing surface waves from teleseismic events [*Rubinstein et al.*, 2007b; *Peng et al.*, 2008] and from afterslip [*Johnson et al.*, 2006].

These properties enable a reassessment of depth-dependent fault zone rheology in relation with the structure and physical state of the fault and the surrounding crust [*Handy et al.*, 2007]. In order to make progress in this question, it is important to characterize structures and fabrics throughout the crustal column. In this paper we focus on the structure of the crust around the San Andreas Fault near Parkfield, California, using teleseismic receiver functions. These data represent an approximation to the Earth's teleseismic Green's function (i.e., impulse response to a teleseismic body wave) and are particularly useful in characterizing deep crustal structure at high resolution [e.g., *Ron-*

denay et al., 2001; *Nabelek et al.*, 2009; *Frassetto et al.*, 2011]. Most applications that use receiver functions typically make simplifying assumptions (i.e., horizontally-layered, isotropic structure) in order to provide first order details of the crust and upper mantle. There is now ample evidence that receiver functions contain much more information on structure from the contribution of seismic anisotropy (i.e., the variations in seismic wave velocity for different directions of propagation) [e.g., *Levin and Park*, 1997; *Savage*, 1998]. This anisotropy can be directly related to either structural heterogeneity (e.g., dipping seismic velocity contrast), stress-induced microcracks, or to tectonic fabric caused by the alignment of anisotropic minerals and rocks. Seismic anisotropy therefore provides crucial information in identifying the relation between fault zone rheology and structure.

In Central California the regional crustal structure is well-known from recent body-wave [e.g., *Thurber et al.*, 2009; *Lin et al.*, 2010] studies that show a sharp contrast in seismic velocities across the San Andreas Fault to a depth of $\sim$15 km, as well as ambient noise tomography [e.g., *Shapiro et al.*, 2005; *Lin et al.*, 2008] studies. Shear-wave splitting analyses from local earthquake data also point to shallow, stress-induced anisotropy as well as layered structural anisotropy on either side of the San Andreas Fault [*Zhang et al.*, 2007a; *Liu et al.*, 2008]. Seismic studies that use receiver functions are comparatively sparse. Of note, *Ozacar and Zandt* [2009] find evidence for a deep, lower crustal low-velocity layer near Parkfield characterized by elastic anisotropy that they interpret as a layer of serpentinite or fluid-filled schists. In comparison, the regional structure of the crust in southern California from receiver functions has been more extensively studied by *Zhu and Kanamori* [2000]; *Yan and Clayton* [2007] and *Porter et al.* [2011]. These studies reveal significant complexity in receiver function waveforms that correlate with

tectonic structures. In particular, *Porter et al.* [2011] performed an inversion of receiver function data using a model with layered anisotropy within the lower crust of southern California. These results suggest that dominant trends in lower crustal anisotropy can be interpreted as a fossilized shear-induced fabric within schists created during pre-transform, early tertiary subduction, thus revealing distributed deformation in the lower crust.

In what follows we provide constraints on the structure and anisotropy of the crust around the San Andreas Fault using data from a dense array of broadband seismic stations deployed near Parkfield, California. In particular we show that receiver functions display strong back-azimuth variations in both timing and amplitude of P-S converted waves that are either due to structural heterogeneity or elastic anisotropy. We then decompose receiver functions into back-azimuth harmonics to help visualize the continuity of crustal structure and anisotropy along profiles. Finally we construct synthetic velocity models of the crust to constrain the origin of the seismic anisotropy. These results yield insight into the role of structure and fabrics in the rheology of the San Andreas Fault.

1.1. Tectonic setting

In Central California near Parkfield, the San Andreas Fault currently separates the largely granitic Salinian block to the southwest from the sedimentary units of the Franciscan Complex to the northeast. The Salinian block is composed mainly of Cretaceous granites overlain by Tertiary marine sedimentary rocks and represents fragments of the batholithic arc that was formerly part of the Sierra Nevada and Peninsular Ranges and were translated northward by the initiation of transform motion along the San Andreas Fault. Rocks of the Franciscan Complex represent an oceanic assemblage of late Cretaceous to early Tertiary mafic material and marine sediments that accreted onto the North

American plate. Lower crustal rocks composing the Central California crust were mostly emplaced during Laramide shallow flat slab subduction that underplated marine sediments of the accretionary complex, which were later metamorphosed into schists [*Ducea et al.*, 2009]. Following the end of flat slab subduction, the hanging wall of the former forearc crust collapsed oceanward and locally exposed small schist outcrops.

2. Methods

2.1. Data preprocessing

Data from this study are obtained from selected broadband stations of the permanent Berkeley Digital Seismic Network (stations SAO and PKD) and the temporary Parkfield Area Seismic Observatory (PASO) experiment that operated between June/July 2001 and October 2002 [*Thurber et al.*, 2003] (Figure 1). These stations are uniformly distributed across the trace of the SAF. Three-component seismograms are collected for all events with magnitude M>5.5 in the epicentral distance range 30°-90° that occurred between 2000 and 2011. The vertical and horizontal components of motion are decomposed into upgoing P, S_V (radial), and S_H (transverse) wave modes to partially remove the effect of the free surface [*Bostock*, 1998] using near-surface velocities of $V_P = 6$ km s^{-1} and $V_S = 3.6$ km s^{-1}. We retain seismograms with P-component signal-to-noise ratios > 7.5 dB over the first 10 seconds in the 0-2 Hz frequency band to obtain high-quality receiver functions. Event coverage is dominated by the western and northern Pacific, Fiji-Tonga, and Central and South American corridors, with good back-azimuth coverage from 125° to 175° and from 225° to 40°, and less regularly sampled otherwise.

2.2. Receiver functions

Individual single-event seismograms are processed using the receiver function method, which employs the P component as an estimate of the source wavelet to deconvolve the S_V and S_H components and recover receiver-side S velocity structure. This procedure is performed using a modified Wiener spectral deconvolution with a regularization parameter calculated from the pre-event co-variant noise spectrum between vertical and horizontal components to reduce contamination from seasonal noise effects [*Audet*, 2010]. Receiver functions are filtered using a second-order Butterworth filter with corner frequencies of 0.05-0.5 Hz. Receiver functions are subsequently stacked into 7.5° back-azimuths and 0.002 $\mathrm{s\,km^{-1}}$ slowness bins.

The first ∼10 seconds of S_V and S_H receiver function time series mainly represent forward scattered P-to-S waves from discontinuities in seismic velocities of the crust and upper mantle. In a layered medium, the timing and amplitude of each converted phase constrain the thickness and V_P/V_S of the overlying column and velocity contrasts at discontinuities, respectively. For isotropic, horizontal layers part of the P wave is converted onto the S_V component and no energy is converted onto the S_H component; S_H component signal therefore represents either structural heterogeneity (e.g. dipping interface), rock anisotropy, or both [*Cassidy*, 1992; *Levin and Park*, 1997; *Savage*, 1998; *Frederiksen and Bostock*, 2000; *Liu and Niu*, 2011]. In either case, periodicity in both the amplitude (in particular, polarity reversals) and the timing of converted S_H phase with back-azimuth is expected. For example, a plane dipping layer will produce a 1-θ (360°) periodicity [*Cassidy*, 1992] in both radial and transverse components, in addition to a 1-θ periodic signal observed at the zero-lag time on the transverse component [*Cassidy*, 1992;

Porter et al., 2011]. This zero-lag periodicity can in fact be used to identify the presence of dipping interfaces. In the case of anisotropy the patterns are more complicated due to the various degrees of symmetry of the elastic tensor and its orientation in space [*Levin and Park*, 1997; *Savage*, 1998; *Frederiksen and Bostock*, 2000].

Figures (2) and (3) show radial and transverse component receiver functions for stations SAO and PKD, respectively, which are located near the surface trace of the San Andreas Fault but outside of the PASO network. There are significant differences in signal between these stations, however neither of them show features expected for horizontally layered, isotropic velocity structure of the crust and upper mantle. Both the radial and transverse components display strong back-azimuth variations in the amplitude and timing of wave conversions. In particular, the extremely high amplitudes and evident back-azimuth variations of the S_H component at both stations indicate pervasive directional structure (either dipping layers and/or anisotropy), consistent with previous findings [*Ozacar and Zandt*, 2009; *Porter et al.*, 2011]. Interestingly, the zero-lag amplitudes of the transverse components do not display a clear periodicity with back-azimuth that would indicate the presence of dipping layers (see Supplementary Material). Although this test does not rule out the presence of dipping layers in the subsurface, it indicates that a single dipping interface or layer is not the dominant source of signal. One main difference between these results and those of *Ozacar and Zandt* [2009] and *Porter et al.* [2011] is the absence of a large positive signal at zero-lag on the radial component, due to the better isolation of the P wave from the modal decomposition and its more complete removal in the deconvolution.

To facilitate visualization of the periodicity in back-azimuth, we perform a harmonic decomposition of the receiver function data [*Shiomi and Park*, 2008; *Bianchi et al.*, 2010]. This technique exploits the coupled back-azimuth variations in the S_V and S_H components to simplify the identification of structural features and to constrain the source of anisotropy in the crust.

2.3. Harmonic decomposition

Prior to performing the decomposition, we migrate S_V and S_H receiver functions to depth using a background velocity model from the P-velocity model of *Lin et al.* [2010], updated by *Zeng et al.* [2014], which we convert to S-velocity using a constant V_P/V_S ratio of 1.73 [*Lin et al.*, 2010]. Because the total aperture of the dense array is small but encompasses both sides of the SAF with large lateral contrasts in velocity, we produce average crustal velocity models corresponding to either side of the SAF. We note that the results presented herein are only weakly dependent on any particular background velocity model. Individual receiver function bins for both S_V and S_H components are migrated to depth using the P to S travel time equation to correct for non-vertical angle of incidence [*Dueker and Sheehan*, 1997]. We select a depth range between 0 and 55 km ($\Delta T_{PS} < 10$ s) to mitigate interference caused by free-surface reverberations of crustal phases. We therefore end up with two sets of receiver function bins (S_V and S_H) at each station, ordered by depth and back azimuth of incoming wavefield.

The harmonic decomposition technique is detailed in *Shiomi and Park* [2008]; *Bianchi et al.* [2010] and *Agostinetti et al.* [2011]. The method exploits the periodic behavior of both radial and transverse components by decomposing receiver functions into a set of back-azimuth harmonics. In particular, the method assumes that at every depth interval,

the set of S_V and S_H amplitudes can be expressed as a sum of $\cos(k\phi)$ and $\sin(k\phi)$, where k is the harmonic degree and ϕ is the back-azimuth. In this work we limit the decomposition to degrees $k = 0, 1, 2$, which constrain most simple models of heterogeneity (i.e., dipping interface) and elastic anisotropy (hexagonal symmetry with slow or fast axis) [*Bianchi et al.*, 2010]. The linear system of equations can be written [*Bianchi et al.*, 2010]

$$\begin{pmatrix} S_{V_1}(z) \\ \vdots \\ S_{V_N}(z) \\ S_{H_1}(z) \\ \vdots \\ S_{H_N}(z) \end{pmatrix} = \begin{pmatrix} 1 & \cos(\phi_1-\alpha) & \sin(\phi_1-\alpha) & \cos(2(\phi_1-\alpha)) & \sin(2(\phi_1-\alpha)) \\ \vdots & & & & \\ 1 & \cos(\phi_N-\alpha) & \sin(\phi_N-\alpha) & \cos(2(\phi_N-\alpha)) & \sin(2(\phi_N-\alpha)) \\ 0 & \cos(\phi_1-\alpha+\frac{\pi}{2}) & \sin(\phi_1-\alpha+\frac{\pi}{2}) & \cos(2(\phi_1-\alpha)+\frac{\pi}{4}) & \sin(2(\phi_1-\alpha)+\frac{\pi}{4}) \\ \vdots & & & & \\ 0 & \cos(\phi_N-\alpha+\frac{\pi}{2}) & \sin(\phi_N-\alpha+\frac{\pi}{2}) & \cos(2(\phi_N-\alpha)+\frac{\pi}{4}) & \sin(2(\phi_N-\alpha)+\frac{\pi}{4}) \end{pmatrix} \begin{pmatrix} A(z) \\ B_\parallel(z) \\ B_\perp(z) \\ C_\parallel(z) \\ C_\perp(z) \end{pmatrix}, \tag{1}$$

where α represents any azimuth of interest. The term A corresponds to the constant part of the S_V component ($k = 0$) with respect to back azimuth. If the medium were made up of isotropic, horizontal layers, A would contain all the energy of the signal without any contribution from higher degrees (see Supplementary Material). This component therefore mainly characterizes the background isotropic structure onto which complexity (heterogeneity, anisotropy) is superimposed. The terms $B_\parallel$ and $B_\perp$ contain information on the 1-θ periodicity ($k = 1$ harmonics) in receiver functions. In the equations above we use a configuration whereby the S_H component is shifted by -$\pi/2$ from the S_V component. The energy of these orthogonal components will depend on α with respect to the back azimuth angles ϕ_i. For example, if $\alpha = 0$ then $B_\parallel$ is oriented N-S and $B_\perp$ is oriented E-W. Therefore, if $\phi_i - \alpha = 0$, then $B_\parallel$ will be maximum and $B_\perp$ will be close to zero. Similarly, the terms $C_\parallel$ and $C_\perp$ contain information on the 2-θ periodicity ($k = 2$ harmonics).

Previous tests with synthetic data have shown that, for simple velocity models with either dipping structure or high order symmetry of elastic anisotropy, the energy is dominant on the first three terms (A, $B_{\|}$ and $B_{\perp}$) and is negligible on the last two terms [*Bianchi et al.*, 2010; *Agostinetti et al.*, 2011] (Supplementary Material). The matrix is inverted using singular value decomposition to solve for the five harmonic components resolved onto a particular azimuth α.

In theory one could invert the above matrix at each depth increment (i.e., $\alpha_i \equiv \alpha(z_i)$) and find the directions α_i for which the energy on one particular harmonic component (except for A) is optimized in some sense. In practice we have found that defining a specific depth range over which the direction α is assumed to be uniform gives more stable results. We use the depth range from the surface to the depth of the predicted Moho from the model of *Lin et al.* [2010]. The matrix is therefore inverted at each depth increment within the specified range for a given value of α, and this procedure is repeated for $\alpha \in 0, 2\pi$. We retain the set of harmonic components for which the variance on the term $B_{\|}$ is minimum. This choice is motivated by the fact that the S_V component is maximum when ϕ_i is at a right angle to the strike of a dipping interface, which corresponds to maximum energy on the $B_{\perp}$ harmonic. The recovered angle, now called α_C, can therefore be intuitively interpreted in terms of the strike of a dipping interface. For anisotropy, synthetic tests show that the orientation of α_C is directly related to the trend of the seismic fast axis of hexagonal anisotropy, or perpendicular to the slow axis. These tests also show how energy varies on each harmonic for dipping structures and anisotropic layering (Supplementary Material).

3. Results

3.1. Individual stations

Figure (4) shows example results for stations SAO and PKD. In both cases we show the harmonic components at the azimuth corresponding to α_C, i.e. where the variance of $B_{\|}$ is minimum. The depth range over which α_C is estimated is shown by the grey shading. For station SAO the recovered azimuth α_C is 316°, and the harmonic components resolved onto this angle show how the signal is separated into the different terms. First, the constant term (A) has low amplitude at all depths, suggesting that isotropic velocity contrasts across horizontal layers are small. In particular, it is unclear which of the two positive pulses at depths of ∼18 km and ∼36 km may be related to the crust-mantle interface. The third component ($B_{\perp}$) contains most of the energy with opposite polarity peaks at ∼5 and ∼15 km depth. The term $B_{\|}$ has low amplitude, implying that the dominant direction (α_C) is uniform within the entire crust. The last two terms $C_{\|}$ and $C_{\perp}$ have low amplitudes, as expected for simple structural models.

Given that the station SAO is close to the trace of the San Andreas Fault with a strike of 321°, the observed partitioning can be intuitively linked with the signature of a dipping interface resolved at depths between 5 and 15 km. In this case the near absence of energy on the term A would suggest that the fault is dipping at a high angle (Supplementary Material), in agreement with the geometry of the SAF. This interpretation is also consistent with a previous receiver function study at station SAO [*Hammer and Langston*, 1996]. However, it is unclear how a near-vertical fault can generate receiver function signals at some distance from the fault trace, or how the crust-mantle interface can become invisible to teleseismic waves. In addition, we do not observe the zero-lag periodicity on the trans-

verse component receiver functions that is associated with dipping layers. Alternatively, if the harmonic signature is related to a ∼10 km thick anisotropic layer located within the crust, the positive pulse on the term $B_\perp$ indicates a fast symmetry axis trending 316°, or a slow symmetry axis trending 226°. Based on a similar variance of the terms A and $C_\perp$, this model would imply a plunge of the anisotropy axis of roughly 50-65° for both cases (Supplementary Material).

For station PKD the situation is more complex. The constant term A has high amplitude, in contrast to that of station SAO. Large positive and negative pulses imply that the crust is characterized by a low-velocity layer located approximately at lower crustal depths, consistent with a recent study [*Ozacar and Zandt*, 2009]. The largest positive peak in A, presumably associated with the crust-mantle interface, is located at a depth of ∼30 km. The term $B_\perp$ is also characterized by high amplitude, alternating positive and negative pulses, suggesting layered anisotropy. The resolved direction α_C is 331°, indicating a fast axis trending 331° or a slow axis trending 241°, in close agreement with the slow axis trend of 236° found by *Porter et al.* [2011] for this station. In addition, the term $B_\parallel$ still contains significant energy, implying that α_C likely varies with depth within the crust. These signals are very difficult to interpret in terms of simple structure and geometry, and require a multi-layered anisotropic model with or without the contribution from dipping interfaces to explain the data. Lower-order symmetry of elastic anisotropy may also be required to explain strong energy on higher-order harmonic terms.

3.2. Crustal structure around the San Andreas Fault

Figure (5a) shows the recovered α_C for all stations of the PASO network located around the San Andreas Fault near Parkfield. The dominant direction in receiver functions

roughly follows the strike of the SAF, with some small-scale variations. These results indicate that the main orientation of crustal fabric or structure is uniform over a large area surrounding the SAF. Since the effects of a steeply dipping structure are expected to vary rapidly away from the fault (see subsection 4.2), this suggests that the source of variations in back-azimuth is likely due to layered anisotropy within the crust. Figure (5b) shows the surface projection of rays piercing virtual interfaces at 10, 20 and 30 km depth around station CVCR, located on the eastern side of the SAF. These points reflect the distribution of slowness and back-azimuth for a typical station of the array, and show that rays beneath each seismic station are sampling both sides of the SAF at various depths, thereby complicating the interpretation of results for individual stations.

Figures (6) and (7) show the results of the A and $B_{\perp}$ terms for stations located along three profiles. In particular, Figure (6a) displays the along-strike variations in both harmonics components for stations located within two kilometers on each side of the profile A-A', following the surface trace of the SAF (Fig. 1a). These data consistently show a faint positive pulse at $\sim$30-40 km depth on the A term that varies along strike, likely associated with the crust-mantle interface. The $B_{\perp}$ term exhibits a prominent positive pulse at shallow depth, similar to the signal observed at station SAO (Fig. 4a). However, only a subset of stations show a deeper ($\sim$15-20 km), negative pulse, and this signal appears discontinuous along strike. To facilitate the visualization of these results, we interpolated the A and $B_{\perp}$ components at each depth increment along the profile and produced pseudo-continuous images of the subsurface (Fig. 6c). These images further enhance the discontinuities and small-scale variations in both harmonic terms.

We further divided the set of results for the profile A-A' into two subsets, according to the location of each station with respect to the surface trace of the SAF. Panels (b) and (e) of Figure (6) show the results for stations to the northeast of the SAF, whereas panels (c) and (f) show results for stations located to the southwest of the SAF. The subdivision into two adjacent profiles clarifies the continuity of crustal structure around the SAF. To the northeast, the crust-mantle interface varies between 30 and 40 km, although station coverage is sparse. The negative pulse on the $B_\perp$ component appears continuous, following the curvature of the Moho but $\sim$15 km shallower. To the southwest, however, the crust-mantle interface appears more flat, and the deep, negative pulse on the $B_\perp$ term is absent, except at the southeastern end of the profile where it is followed by a second double-polarity pulse immediately below. We note that data from each individual station shown in Figure (6) sample the crust on both sides of the SAF at various depths, thus potentially complicating interpretation based on these images.

Figure (7) shows the results of the A and $B_\perp$ terms along the two profiles oriented perpendicular to the SAF (Fig. 1b). Despite their proximity along strike of the SAF, these profiles exhibit marked differences in recovered structure. In particular, the crust-mantle interface appears to curve significantly on each side of the SAF, and structure observed on the $B_\perp$ component differs markedly on both profiles. Interestingly, the signals observed previously on station PKD (Fig. 4b) can be seen at distinct locations (e.g., at a distance of -4 km on profile B-B' and distance of -6 to -4 km on profile C-C').

Figure (8) shows a pseudo-3D rendering of the A and $B_\perp$ components along the three profiles that highlight the presence of the anisotropic structure around the SAF. Question marks indicate regions where structure is discontinuous. These results facilitate the visu-

alization of the variability in crustal structure around the San Andreas Fault, but do not provide quantitative constraints on structure and anisotropy. On the other hand, they confirm that the crust cannot be represented as a stack of isotropic, horizontal layers. In the next section we examine a range of models that may explain the essential features of the receiver functions. In particular, we draw our attention to two key characteristics of the $B_\perp$ component images: 1) the shallow, positive pulse present at all stations; and 2) the deeper, negative pulse that is absent to the southwest and adjacent to the SAF, but follows the interpreted crust-mantle interface approximately 5-10 km shallower.

4. Modeling and numerical simulations

Because the crust around a major fault zone is likely highly complex, we examine two models of the crust that are meant to represent end-member cases (Figure 9). In the first case (Fig. 9a), the crust is modeled as horizontal layers overlying an isotropic mantle half-space. We further test two variants of the layered model based on the observations above: upper crustal anisotropy, and bi-layered (upper and mid-crustal) anisotropy. In the second end-member case (Fig. 9b), the model is defined as a thin vertical low-velocity zone embedded within an otherwise homogeneous and isotropic crust underlain by an isotropic mantle half-space.

We use two different modeling strategies to obtain synthetic receiver functions that can be compared with observed data. For the first set of models, we use a ray-based fast modeling technique [*Frederiksen and Bostock*, 2000] embedded within a Monte Carlo inversion scheme to obtain parameters for layered crustal anisotropy. The ray-based technique fails to reproduce finite wave effects such as diffraction and wave guides from the wave interactions with a low-velocity fault that could interfere with direct arrivals, and

is therefore not suited for modeling a vertically dipping fault. For the second model we use a waveform modeling technique based on the one-way wave equation [*Audet et al.*, 2007] that correctly reproduces finite-frequency effects. In each case we model waveforms for a set of plane waves with the epicentral and back-azimuth distribution representing that collected at station SAO. Synthetic waveforms are subsequently processed to obtain receiver functions that are directly compared with observed data at station SAO. This station was chosen for the modeling due to its good back-azimuth and slowness coverage and the relative simplicity of the receiver function signals, in order to obtain the best representative set of model parameters. The similarity between the harmonic components of station SAO with those of the PASO network indicates that structural properties of the crust around Parkfield may be explained as spatial variations of the model parameters.

4.1. Layered anisotropy

Models of layered anisotropy tend to produce double-polarity signals similar to those observed at stations located to the northeast of the SAF (Fig. 6b). For stations located to the southwest of the SAF we observe a single pulse at shallow levels without the deeper, opposite polarity arrival (Fig. 6c). This case likely represents a single layer of anisotropy in the upper crust. To examine the two different cases, we fix all background P and S velocities and search for the thickness of 1) an upper crustal anisotropic layer; and 2) both upper and mid crustal anisotropic layers, as well as the parameters characterizing the anisotropy (percent anisotropy, trend and plunge of the symmetry axis; Table 1). For each case we generate 1500 models with pseudo-random sets of parameters. At each iteration we propagate a set of plane waves through the model, calculate receiver functions and evaluate the misfit with data observed at station SAO using a normalized correlation

scheme that includes both radial and transverse components. Cumulative variance within each observed receiver function bin is used as an inverse weight in the misfit calculation and the Monte Carlo inversion for model parameters is carried out using a Neighborhood Algorithm [*Sambridge*, 1999a]. Model appraisal is performed by calculating Bayesian integrals to produce formal estimation errors from posterior probabilities [*Sambridge*, 1999b]. Each case is presented separately below.

4.1.1. Upper crustal anisotropy

Supplementary Figure (S2) shows the results of the inversion. Note that negative anisotropy indicates a slow axis of hexagonal symmetry. Models with a fast axis of symmetry showed much larger misfit values and were discarded for clarity. The best-fitting model (Table 1) reproduces some of the main features of the data, in particular the early ($\sim$1 sec) S_V and S_H signals with periodic variations in polarity. However, the synthetic data do not match the high amplitude of the observed data, suggesting larger velocity/anisotropy contrasts at shallow levels. The misfit panels show a well-sampled parameter space and the various trade-offs between model parameters. The trend of the slow axis is $45^\circ \pm 7^\circ$, perpendicular to α_C, with a plunge of $48^\circ \pm 4^\circ$. This implies that the plane of fast velocities strikes at 138°, parallel to the strike of the SAF, and has a dip of $\sim$42°. The amplitude of the anisotropy is also quite large ($\leq$-30%) but this parameter is not well constrained by the inversion and trades-off with layer thickness, which varies between 2 and 4 km. Previous studies [e.g. *Porter et al.*, 2011] have shown that the percentage of anisotropy and plunge of the symmetry axis are sensitive to the azimuthally-dependent amplitude and delays of arrivals in receiver functions, whereas the trend of the symmetry

axis is sensitive to robustly determined back-azimuth polarity flips in both radial and transverse components.

4.1.2. Bi-layered anisotropy

In this model we introduce an additional mid-crustal anisotropic layer and jointly search for the thickness and anisotropic parameters of both crustal layers. Results are shown in Supplementary Figure (S3) and Table (1). This model successfully reproduces the double polarity pulses on the two components as well as the amplitudes. The best fit model is characterized by a 3.9 ± 1.8 km thick upper crustal layer with $-46 \pm 29\%$ anisotropy and a trend and plunge of $45^\circ \pm 43^\circ$ and $49^\circ \pm 22^\circ$, respectively, and a 8.8 ± 2.9 km thick mid crustal layer with $-27 \pm 22\%$ anisotropy and a trend and plunge of $222^\circ \pm 52^\circ$ and $52^\circ \pm 22^\circ$, respectively. The uncertainty on these estimates are much larger compared with the previous case, however this is likely due to the larger number of estimated parameters and the non-uniqueness in estimating anisotropic parameters for more than one layer.

When decomposed onto the various harmonics (Fig. 10a), the synthetic data reproduce the double polarity pulse on the $B_\perp$ term, with insignificant energy on the A term. Notice however how the Moho depth is correctly determined by the A component. An interpolated image based on these results (Fig. 10c) would therefore show these signals continuously along the profile.

4.2. Vertical low-velocity zone

To model structural heterogeneity we employ a 2.5D modeling code based on the one-way wave equation [*Thomson*, 1999] as described by *Audet et al.* [2007]. Even though the model is two-dimensional, we can reproduce 3D wave effects by modeling wave propagation out of the model plane. The model is defined as a vertical, 3 km wide low-velocity, high

V_P/V_S (equal to 2.1) zone embedded within an otherwise homogeneous, 30 km thick crust underlain by a mantle half-space. Note that this modeling effort is only meant as a test of the fault zone model, and we do not attempt to optimize any model parameter through an inverse procedure. We produce synthetic three-component data by propagating the same set of plane waves through the model, and calculate receiver functions on the synthetic data (not shown) at any desired location along the surface of the 2D model. We then decompose the receiver functions into the various back-azimuth harmonics.

Figure (10b) shows the results for a surface point located 3 km from the center of the fault representing station SAO. The synthetic data reproduce a single positive and early pulse on the $B_\perp$ term, however the amplitude is much too small compared with the signal at station SAO. The energy on the A term shows an early positive pulse, with no apparent signal associated with a crust-mantle interface. This is likely caused by various interference effects between Moho and off-fault conversions that could partly explain the lack of Moho conversion observed at station SAO.

Figure (10d) shows a virtual profile of stations across the surface trace of the SAF. The amplitudes are scaled up three times to visually reproduce the patterns. In the harmonic decomposition the direction of α_C is fixed to the strike of the SAF. Interestingly, the patterns observed on the $B_\perp$ term are flipped in polarity on each side of the fault, without any significant change on the A term. These results indicate that a low-velocity fault model cannot, by itself, reproduce the main features of observed receiver functions around the SAF.

4.3. Summary and caveats

Although these models represent end-member cases and are non-unique, the layered crustal anisotropy model is clearly favored by our receiver function data. The estimates for the anisotropic layers represent structural parameters obtained for data collected at station SAO, which may not be appropriate for the structure beneath the PASO network and likely represent upper bounds. However, we can draw three conclusions from the inversion results. First, stations for which a single early pulse is observed on the $B_\perp$ term may be described by a shallow and thin upper crustal anisotropic layer within an otherwise isotropic crust. Second, stations that display a double polarity pulse on the $B_\perp$ component can be characterized either by a mid crustal anisotropic layer, or the superposition of two anisotropic layers with an opposite sense of dipping slow anisotropy. Finally, where resolved, the depth interval between the two resolved pulses on the $B_\perp$ component is proportional to the thickness of the mid crustal anisotropic layer. When displayed as an interpolated image (e.g., Fig. 10b), as observed in Figure (8), the variability in the double-pulse depth interval can therefore be interpreted as changes in the thickness of the mid crustal anisotropic layer.

We note here that the lower-crustal anisotropy model proposed by *Ozacar and Zandt* [2009] and *Porter et al.* [2011] can be related to the results presented above by considering the variations in the depth range and thickness of the anisotropic layer as evidenced by lateral variations in the harmonic components (Fig. 8).

5. Interpretation

The results obtained here suggest that the crust is highly anisotropic across the San Andreas Fault near Parkfield, California. Seismic anisotropy in the crust is most commonly

attributed to aligned joints or microcracks, lattice preferred orientation of anisotropic minerals, or highly foliated metamorphic rocks [e.g., *Liu and Niu*, 2011; *Bostock and Christensen*, 2012]. In this section we explore various sources of anisotropy that may explain our data.

5.1. Crack-induced anisotropy

Distribution of stress-aligned fluid-filled microcracks are expected in the crust [*Crampin*, 1987]. Microcracks are formed either through stress-induced sub-critical crack growth processes, via hydraulic fracturing in prograde metamorphic reactions [*Crampin*, 1987]. In the first case, cracks are expected to align perpendicular to the minimum principal compressive stress direction [e.g., *Boness and Zoback*, 2006]. This process may induce seismic anisotropy only at low confining pressure where cracks can remain open. Similarly, prograde metamorphic reactions release chemically bound water, which increases in situ pore-fluid pressure and lead to hydraulic fracturing and the formation of inter- and intra-granular microcracks that will again align normal to the minimum principal compressive stress direction [*Crampin*, 1987]. However, although their geometry may be modified by changes in the stress field, cracks formed by such process are not directly stress induced and may be more widespread within the crust. At depths of 6 to 20 km, however, corresponding approximately to confining pressures of 150 to 530 MPa, widespread microcracks would require extremely high (i.e., near lithostatic) pore-fluid pressures capped by a low-permeability seal.

Crack-induced anisotropy tends to produce a slow axis of hexagonal symmetry oriented normal to the crack alignment. Most studies use the spitting between two orthogonally polarized shear waves (i.e., shear-wave splitting) from local earthquakes to determine the

orientation of pervasive microcracks [e.g., *Boness and Zoback*, 2006; *Li et al.*, 2014]. In this case the orientation of the fast polarization would lie parallel to the aligned cracks. However, these data only resolves the surface projection (i.e., trend) of fast and slow axes of shear-wave propagation, which introduces an ambiguity in the determination of their orientation in 3D. The inversion of receiver function data, as performed here, is better suited to recover both the trend and plunge of the anisotropic slow axis and provide a direct test of the crack-induced hypothesis.

Assuming that our results reflect fluid-filled, crack-induced anisotropy in the upper crust, and that such cracks reflect the current stress field, the orientation of the slow axis of symmetry implies a minimum principal stress oriented sub-vertically, in contradiction with stress measurements [e.g., *Hardebeck and Hauksson*, 1999]. It is thus difficult to reconcile our seismic observations with crack-induced anisotropy, unless the ∼5-10 km thick layer was formed in a different stress field and remained intact under the current stress field. If this were the case, the required presence of near-lithostatic pore-fluid pressures in the mid crust would be consistent with the high electrical conductivity around Parkfield [*Becken et al.*, 2011]. However, the consistent orientation of the slow axis of anisotropy across both sides of the San Andreas Fault (Fig. 5a) in two distinct geologic terranes argues against this hypothesis.

Alternatively, upper crustal anisotropy may be caused by the alignment of macroscopic fractures due to shear-induced deformation away from the main fault trace [*Boness and Zoback*, 2006]. This type of structural anisotropy tends to produce fault-parallel fast polarizations around major faults. This type of shear fabric is expected to be confined laterally to the damage zone, a few hundred meters from the fault trace. It is unclear,

499 however, how such a shear-induced fabric would produce a sharp discontinuity observable
500 using receiver function data, unless the maximum depth reflected the maximum confining
501 pressure at which fractures remain open. The observed lateral extent (>3 km) of the upper
502 crustal anisotropic layer is also difficult to reconcile with shear-induced crustal fabric.

5.2. Rock-induced anisotropy

503 Another possible source of crustal anisotropy is the alignment of anisotropic minerals
504 due to distributed shear deformation. In the Central California crust, we expect to find
505 pervasive micaceous schists with a well-defined foliation that reflects the sense of shear
506 during emplacement. The regional alignment of mica into a single foliation is the dominant
507 contributor to the generation of crustal seismic anisotropy characterized by a slow axis of
508 hexagonal symmetry oriented perpendicular to the foliation [e.g. *Lloyd et al.*, 2009, 2011].
509 In particular, single crystal velocity properties of muscovite and biotite micas can reach
510 >50% [e.g. *Ward et al.*, 2012]. The anisotropy of rock aggregates containing mica and
511 quartz minerals is more complex, with greater anisotropy obtained for aggregates contain-
512 ing >20% mica [*Dempsey et al.*, 2011; *Ward et al.*, 2012; *Erdman et al.*, 2013]. Assuming
513 that our results represent anisotropy due to the alignment of mica-rich foliations in schist
514 packages, the orientation of the slow axis is consistent with their emplacement during flat
515 slab subduction [*Porter et al.*, 2011]. This implies that the mid crustal layer remained
516 intact during the subsequent rotation and translation of the crustal blocks along the San
517 Andreas Fault. This would imply that the schists represent a fossilized, strong fabric that
518 is well coupled with the upper crust [*Ozacar and Zandt*, 2009; *Porter et al.*, 2011].

519 Alternatively, our results may also represent anisotropy due to serpentinites that origi-
520 nate either from the paleo-oceanic plate or hydrated mantle wedge and were later sheared

and underplated to the base of the North American crust [*Ozacar and Zandt*, 2009]. The low-temperature, low-pressure serpentine minerals lizardite and antigorite can produce significant anisotropy (>50%) that can be approximated by hexagonal symmetry with a slow axis corresponding to the crystallographic c axis [*Mainprice and Ildefonse*, 2009; *Watanabe et al.*, 2011]. The fossilized sense of shear inferred from the alignment of the slow axis of anisotropy with former subduction underplating, implying the preservation of mid crustal fabric, is more difficult to reconcile with a serpentinite layer. The presence of serpentinite can significantly reduce the integrated strength of the lithosphere [*Escartin et al.*, 1997], which would tend to localize deformation to the weak serpentinite layer, and therefore realign its fabric to NW-SE directed shear-induced lower crustal flow during translation of the crustal blocks. However this effect may be localized the thin shear zone, and we cannot discard serpentinites as a possible source of mid crustal anisotropy.

6. Discussion

Our results, summarized in Figure (11), reveal the complexity of crustal structure around the San Andreas Fault, with possible implications for the rheology of the crust and fault zone. At shallow depth the deformation of the crust is controlled by brittle processes and we interpret the upper crustal anisotropy at depth ∼5-10 km to be caused by open microcracks or aligned fracture network, although other interpretations are possible. The width of the anisotropic zone extends to >3 km away from the surface fault trace, which is much wider than the 100-300 m of low-velocity damage zone inferred from fault zone trapped waves but similar to results found near the North Anatolian Fault [*Li et al.*, 2014] and the Denali Fault [*Rasendra et al.*, 2014]. This result suggests that fault-related micro-cracks may exist at large distances from the fault. Unlike the results for the North

Anatolian Fault, however, the upper crustal layer of anisotropy is observed symmetrically on both sides of the San Andreas Fault. The depth extent of the interpreted fractured layer is compatible with the majority of earthquakes on the San Andreas Fault occurring at shallow depth, which tend to be clustered around the bottom of the upper crustal anisotropic discontinuity (Fig. 6). This depth is also reported in other studies [e.g., *Liu et al.*, 2004, 2008; *Rasendra et al.*, 2014; *Zhang et al.*, 2007b]. The high amplitude of anisotropy and high confining pressure suggest that elevated pore-fluid pressure may be required to maintain cracks or fractures open. The presence of high pore-fluid pressures within a fractured medium around the San Andreas Fault may reduce its brittle strength and localize slip along the fault zone.

The depth extent of the San Andreas Fault, and the nature of deformation in the middle to lower crust, can be examined using our data. At those depths, our results indicate the presence of a strongly anisotropic layer sandwiched between the upper crustal layer and the Moho (Fig. 8). There is also a marked contrast in crustal anisotropy across the San Andreas Fault at depth >10 km, suggesting that deformation may be partitionned between the two adjacent crustal blocks (Fig. 6). We interpret the source of anisotropy as pervasive and highly foliated mica schists or serpentinites. Our results are consistent with those of *Wilson et al.* [2004], who interpret the presence of an unbroken Moho and pervasive lower crustal anisotropy around the Alpine Fault in New Zealand as evidence of distributed deformation as opposed to a discrete shear zone. However, the large contrast in anisotropy across the fault from the surface to ∼35 km depth provides indirect evidence of a shear zone cutting the entire crust [*Zhu*, 2000]. This result also suggests that the development of anisotropy at those depths may predate strike-slip faulting [*Porter et al.*,

2011]. Alternatively, the difference in anisotropy on each side of the SAF may indicate a contrast in strength across the fault.

Crustal thickness is seen to vary between 30 and 40 km with no apparent discontinuity across the SAF. These Moho depths are inconsistent with early reports by *Walter and Mooney* [1982]; *Fuis* [1998] and *Page et al.* [1998], who find crustal reflectors at ∼25 km. *Trehu and Wheeler* [1987] observed a deep reflective band across the SAF that they interpret as a wedge of subducted sediments at ∼20 km depth. According to our results, these reflectors may coincide with the base of the mid-crustal anisotropic layer, although the spatial extent of our receiver function results is much smaller. In a recent study, *Bleibinhaus et al.* [2007] resolve an intermittent mid-crustal discontinuity at ∼10 km depth within the Salinian Terrane to the southwest of the SAF that they interpret as a fluid-rich horizon within layers of metasedimentary rocks. This discontinuity is suggested to represent fluid lubricated shear zones that potentially decouple upper and lower crust and coincide with the depth to brittle-ductile transition. Out results agree remarkably well with these findings, and strongly suggest that structure is closely linked with the rheology of the crust.

A key constraint on rheological processes occurring in the deep extension of the SAF is related to the presence of slow fault slip in the form of tectonic tremors and low-frequency earthquakes (LFEs) [*Nadeau and Dolenc*, 2005; *Shelly and Hardebeck*, 2010]. Tremors and LFEs are thought to occur near the transition from velocity-weakening to velocity-strenghthening slip along the fault zone [*Johnson et al.*, 2013]. This transition may or may not coincide with the brittle-ductile transition describing the change in rheological processes as a function of pressure and temperature in the crust. The spatial gap between

589 regular earthquakes and LFEs and the narrow depth range of LFEs in the lower crust
590 are difficult to reconcile with a change from brittle to ductile deformation. According to
591 our results, LFEs are mostly located within the mid crustal anisotropic layer, to the NE
592 side of the SAF, although the uncertainty of LFE epicenters is on the order of 2 km (D.
593 Shelly, personal communication). Nevertheless, the coincidence of LFEs with the contrast
594 in lower crustal anisotropy across the SAF suggests that LFEs may be partly controlled
595 by the presence of weak minerals such as mica or serpentine.

596 Field evidence suggests that episodic slow fault slip may be caused by weak anisotropic
597 fabric in a fluid-overpressured, heterogeheous shear zone [*Fagereng et al.*, 2010]. Fluid
598 overpressures may arise from the dehydration of a serpentinite body in the upper mantle,
599 given realistic permeability anisotropy and NE dipping faults as well as fractures within
600 the country rock [*Fulton and Saffer*, 2009]. The presence of fluids is also indicated by
601 low electrical resistivity [*Becken et al.*, 2011], evidence of dynamic tremor triggering by
602 teleseismic surface waves *Peng et al.* [2008] and solid Earth tides [*Thomas et al.*, 2009],
603 and is suggested from simulations of tremor-related creep [*Johnson et al.*, 2013] that
604 require extremely low effective normal stress. Our results suggest that the weakness of
605 the San Andreas Fault is likely due to the presence of fluid-rich layers of intrinsically weak
606 anisotropic minerals inherited from previous tectonic events.

7. Conclusion

607 In this paper we use teleseismic receiver functions to characterize the structure of the
608 crust around a portion of the San Andreas Fault near Parkfield, California. These data
609 indicate that the crust is highly anisotropic and can be modeled by one or more layers
610 of seismic anisotropy with thicknesses that vary laterally along and across the fault. The

upper crustal layer has very large anisotropy characterized by a slow axis of hexagonal symmetry, and may be interpreted as a fluid-rich zone containing aligned micro-cracks. The mid-crustal layer is more prominent on the northeast side of the SAF, and is characterized by lower anisotropy with a slow axis of symmetry that is oriented in the opposite direction from the upper layer, and may represent a fluid-rich layer containing a large amount of aligned mica or serpentine minerals. These results suggest that the weakness of the San Andreas Fault may be due to the combination of elevated fluid pressures within sheared layers of intrinsically weak anisotropic rocks.

The model presented herein is certainly not unique. In particular it is difficult to determine the exact source of anisotropy at depth in geologically complex areas. Future efforts should be directed toward mapping out crustal structures at a larger scale across and along the San Andreas Fault in order to constrain the origin and relation of these layers to both the geological history and rheology of the shear zone. Additional insight may also come from the comparison of these structures with those observed at other continental transform faults, such as the North Anatolian and Alpine faults.

Acknowledgments. The author would like to thank N. Piana Agostinetti for sharing the harmonic decomposition software, and R. Bürgmann, T. Taira, R. Nadeau, I. Johansson and R. Turner for discussions on various aspects of this work. Careful reviews by R. Porter and an anonymous reviewer improved this paper. Figure 1 was produced with the help of C. Amos. The software RAYSUM and the Neighborhood Algorithm, by A. Frederiksen and M. Sambridge, respectively, were used to calculate synthetic data for the layered anisotropy models. The software ONE_WAY was used to model waveforms for the dipping models. All figures were prepared using the Generic Mapping Tool soft-

ware. This work is supported by the Natural Science and Engineering Research Council of Canada. The facilities of the IRIS Data Management System, and specifically the IRIS Data Management Center, were used for access to waveform and metadata required in this study (http:// www.iris.edu/mda/XN). The IRIS DMS is funded through the National Science Foundation and specifically the GEO Directorate through the Instrumentation and Facilities Program of the National Science Foundation under Cooperative Agreement EAR-1063471. Seismic data were also obtained from the Northern California Earthquake Data Center (http://service.ncedc.org/).

References

Agostinetti, N. P., I. Bianchi, A. Amato, and C. Chiarabba, Fluid migration in continental subduction: The Northern Apennines case study, *Earth Planet. Sci. Lett.*, *302*, 267–278, 2011.

Audet, P., Temporal variations in crustal scattering structure near Parkfield, California, using receiver functions, *Bull. Seism. Soc. Am.*, *100*, 1356–1362, 2010.

Audet, P., M. G. Bostock, and J.-P. Mercier, Teleseismic waveform modelling with a one-way wave equation, *Geophys. J. Int.*, *171*, 1212–1225, doi:10.1111/j.1365–246X.2007.03,586.x, 2007.

Becken, M., O. Ritter, P. A. Debrosian, and U. Weckmann, Correlation between deep fluids, tremor and creep along the central San Andreas Fault, *Nature*, *480*, 87–90, 2011.

Beroza, G. C., and S. Ide, Slow earthquakes and nonvolcanic tremor, *Annu. Rev. Earth Planet. Sci.*, *39*, 271–296, 2011.

Bianchi, I., J. Park, N. P. Agostinetti, and V. Levin, Mapping seismic anisotropy using harmonic decomposition of receiver functions: An application to Northern Apennines, Italy, *J. Geophys. Res.*, *115*, B12,317, doi:10.1029/2009JB007,061, 2010.

Bleibinhaus, F., J. A. Hole, T. Ryberg, and G. S. Fuis, Structure of the California Coast Range and San Andreas Fault at SAFOD from seismic waveform inversion and reflection imaging, *J. Geophys. Res.*, *112*, B06,315, 2007.

Boness, N. L., and M. D. Zoback, Mapping stress and structurally controlled crustal shear velocity anisotropy in California, *Geology*, *34*, 825–828, 2006.

Bostock, M. G., Mantle stratigraphy and evolution of the Slave province, *J. Geophys. Res.*, *103*, 21,183–21,200, 1998.

Bostock, M. G., and N. I. Christensen, Split from slip and schist: Crustal anisotropy beneath northern Cascadia from non-volcanic tremor, *J. Geophys. Res.*, *117*, B08,303, doi:10.1029/2011JB009,095, 2012.

Cassidy, J. F., Numerical experiments in broadband receiver function analyses, *Bull. Seism. Soc. Am.*, *82*, 1453–1474, 1992.

Crampin, S., Geological and industrial implications of extensive-dilatancy anisotropy, *Nature*, *328*, 491–496, 1987.

Dempsey, E. D., D. J. Prior, R. Mariani, V. G. Toy, and D. J. Tatham, Mica-controlled anisotropy within mid-to-upper crustal mylonites: an EBSD study of mica fabrics in the Alpine Fault Zone, in *Deformation Mechanisms, Rheology and Tectonics: Microstructures, Mechanics and Anisotropy*, vol. 360, edited by D. J. Prior, E. H. Rutter, and D. J. Tatham, pp. 33–48, Geological Society, London, Special Publications, 2011.

Ducea, M. N., S. Kidder, J. T. Chesley, and J. B. Saleeby, Tectonic underplating of trench sediments beneath magmatic arcs: the central California example, *Int. Geol. Rev.*, *51*, 1–26, 2009.

Dueker, K. G., and A. F. Sheehan, Mantle discontinuity structure from midpoint stacks of converted P to S waves across the Yellowstone hotspot track, *J. Geophys. Res.*, *102*, 8313–8327, 1997.

Erdman, M. E., B. R. Hacker, G. Zandt, and G. Steward, Seismic anisotropy of the crust: Electron-backscatter diffraction measurements from the Basin and Range, *Geophys. J. Int.*, *95*, 1211–1229, 2013.

Escartin, J., G. Hirth, and B. Evans, Effects of serpentinization on the lithospheric strength and the style of normal faulting at slow-spreading ridges, *Earth Planet. Sci. Lett.*, *151*, 181–189, 1997.

Fagereng, A., F. Remitti, and R. H. Sibson, Shear veins observed within anisotropic fabric at high angles to the maximum compressive stress, *Nat. Geosci.*, *3*, 482–485, 2010.

Frassetto, A. M., G. Zandt, H. Gilbert, T. J. Owens, and C. H. Jones, Structure of the Sierra Nevada from receiver functions and implications for lithospheric foundering, *Geosphere*, *7*, 898–921, doi:10.1130/GES00,570.1, 2011.

Frederiksen, A. W., and M. G. Bostock, Modelling teleseismic waves in dipping anisotropic structures, *Geophys. J. Int.*, *141*, 401–412, 2000.

Fuis, G. S., West margin of North America - A synthesis of recent transects, *Tectonophysics*, *288*, 265–292, 1998.

Fulton, P. M., and D. M. Saffer, Potential role of mantle-dericed fluids in weakening the San Andreas Fault, *J. Geophys. Res.*, *114*, B07,408, 2009.

Fulton, P. M., D. M. Saffer, R. N. Harris, and B. A. Bekins, Re-evaluation of heat flow data near Parkfield, CA: Evidence for a weak San Andreas Fault, *Geophys. Res. Lett.*, *31*, L15S15, 2004.

Hammer, J. K., and C. A. Langston, Modeling the effect of San Andreas Fault structure on receiver functions using elastic 3D finite difference, *Bull. Seism. Soc. Am.*, *86*, 1608–1622, 1996.

Handy, M. R., and J.-P. Brun, Seismicity, structure and strength of the continental lithosphere, *Earth Planet. Sci. Lett.*, *223*, 427–441, 2004.

Handy, M. R., G. Hirth, and N. Hovius (Eds.), *Tectonic Faults: Agents of change on a dynamic Earth*, MIT Press, Cambridge, Mass., 2007.

Hardebeck, J., and E. Hauksson, Role of fluids in faulting inferred from stress field signatures, *Science*, *285*, 236–239, 1999.

Johnson, K. M., R. B urgmann, and K. Larson, Frictional properties on the San Andreas Fault near Parkfield from models of afterslip following the 2004 earthquake, *Bull. Seism. Soc. Am.*, *96*, S321–S338, 2006.

Johnson, K. M., D. R. Shelly, and A. M. Bradley, Simulations of tremor-related creep reveal a weak crustal root of the San Andreas Fault, *Geophys. Res. Lett.*, *40*, 1300–1305, 2013.

Lachenbruch, A. H., and J. H. Hass, Heat flow and energetics of the San Andreas fault zone, *J. Geophys. Res.*, *85*, 6185–6222, 1980.

Levin, V., and J. Park, P-SH conversions in a flat-layered medium with anisotropy of arbitrary orientation, *Geophys. J. Int.*, *131*, 253–266, 1997.

721 Li, Z., H. Zhang, and Z. Peng, Structure-controlled seismic anisotropy along the Karadere-
722 D uzce branch of the north anatolian fault revealed by shear-wave splitting tomography,
723 *Earth Planet. Sci. Lett.*, *391*, 319–326, 2014.

724 Lin, F., M. P. Moschetti, and M. H. Ritzwoller, Surface wave tomography of the western
725 United States from ambient seismic noise: Rayleigh and Love wave phase velocity maps,
726 *Geophys. J. Int.*, *173*, 281–298, 2008.

727 Lin, G., C. H. Thurber, H. Zhang, E. Hauksson, P. M. Shearer, F. Waldhauser, T. M.
728 Brocher, and J. Hardebeck, A California statewide three-dimensional seismic velocity
729 model from both absolute and differential times, *Bull. Seism. Soc. Am.*, *100*, 225–240,
730 2010.

731 Liu, H., and F. Niu, Estimating crustal seismic anisotropy with a joint analysis of radial
732 and transverse receiver function data, *Geophys. J. Int.*, *188*, 144–164, 2011.

733 Liu, Y., T.-L. Teng, and Y. Ben-Zion, Systematic analysis of shear-wave splitting in the
734 aftershock zone of the 1999 Chi-Chi, Taiwan, earthquake, *Bull. Seism. Soc. Am.*, *94*,
735 2330–2347, 2004.

736 Liu, Y., H. Zhang, C. Thurber, and S. Roecker, Shear-wave anisotropy in the crust around
737 the San Andreas Fault near parkfield: spatial and temporal analysis, *Geophys. J. Int.*,
738 *172*, 957–970, 2008.

739 Lloyd, G. E., R. W. H. Butler, M. Casey, and D. Mainprice, Mica, deformation fabrics and
740 the seismic properties of the continental crust, *Earth Planet. Sci. Lett.*, *288*, 320–328,
741 2009.

742 Lloyd, G. E., R. W. H. Butler, M. Casey, D. J. Tatham, and D. Mainprice, Constraints
743 on the seismic properties of the middle and lower continental crust, in *Deformation*

Mechanisms, Rheology and Tectonics: Microstructures, Mechanics and Anisotropy, vol. 360, edited by D. J. Prior, E. H. Rutter, and D. J. Tatham, pp. 7–32, Geological Society, London, Special Publications, 2011.

Mainprice, D., and B. Ildefonse, Seismic anisotropy of subduction zone minerals - Contribution of hydrous phases, in *Subduction zone geodynamics*, edited by S. Lallemand and F. Funiciello, Frontiers in Earth Sci., pp. 63–84, Springer, Berlin, Germany, 2009.

Moore, D. E., and M. J. Rymer, Talc-bearing serpentinite and the creeping section of the San Andreas fault, *Nature*, *448*, 795–797, 2007.

Nabelek, J., G. Hetenyi, J. Vergne, S. Sapkota, B. Kafle, M. Jiang, J. Chen, B.-S. Huang, and the Hi-CLIMB team, Underplating in the Himalaya-Tibet collision zone revealed by the Hi-CLIMB experiment, *Science*, *325*, 1371–1374, 2009.

Nadeau, R. M., and D. Dolenc, Nonvolcanic tremors deep beneath the San Andreas Fault, *Science*, *307*, 389, 2005.

Ozacar, A. A., and G. Zandt, Crustal structure and seismic anisotropy near the San Andreas Fault at Parkfield, California, *Geophys. J. Int.*, *178*, 1098–1104, doi:10.1111/j.1365,246X.2009.04,198, 2009.

Page, B. M., G. A. Thompson, and R. G. Coleman, Late Cenozoic tectonics of the central and southern Coast Ranges of California, *Geol. Soc. Am. Bull.*, *110*, 846–876, 1998.

Peng, Z., and J. Gomberg, An integrated perspective of the continuum between earthquakes and slow-slip phenomena, *Nat. Geosci.*, *3*, 599–607, 2010.

Peng, Z., J. E. Vidale, K. C. Creager, J. L. Rubinstein, J. Gomberg, and P. Bodin, Strong tremor near Parkfield, CA, excited by the 2002 Denali Fault earthquake, *Geophys. Res. Lett.*, *35*, L23,305, 2008.

767 Porter, R., G. Zandt, and N. McQuarrie, Pervasive lower-crustal seismic anisotropy in
768 Southern California: Evidence for underplated schists and active tectonics, *Lithosphere*,
769 *3*, 201–220, 2011.

770 Rasendra, N., M. Bonnin, S. Mazzotti, and C. Tiberi, Crustal and upper-mantle
771 anisotropy related to fossilized transpression fabric along the Denali Fault, northern
772 Canadian Cordillera, *Bull. Seism. Soc. Am.*, *104*, 1964–1975, 2014.

773 Rondenay, S., M. G. Bostock, and J. Shragge, Multiparameter two-dimensional inversion
774 of scattered teleseismic body-waves. 3: Application to the Cascadia 1993 data set,
775 *J. Geophys. Res.*, *106*, 30,795–30,807, 2001.

776 Rubinstein, J. L., M. La Rocca, J. E. Vidale, K. Creager, and A. G. Wech, Tidal modu-
777 lation of nonvolcanic tremor, *Science*, *319*, 186–189, 2007a.

778 Rubinstein, J. L., J. E. Vidale, J. Gomberg, P. Bodin, K. C. Creager, and S. D. Malone,
779 Non-volcanic tremor driven by large transient shear stresses, *Nature*, *448*, 579–582,
780 doi:10.1038/nature06,017, 2007b.

781 Sambridge, M., Geophysical inversion with a Neighbourhood Algorithm -I. Searching a
782 parameter space, *Geophys. J. Int.*, *138*, 479–494, 1999a.

783 Sambridge, M., Geophysical inversion with a Neighbourhood Algorithm -II. Appraising
784 the ensemble, *Geophys. J. Int.*, *138*, 727–746, 1999b.

785 Sass, J. H., C. F. Williams, A. H. Lachenbruch, S. P. G. Jr, and F. V. Grubb, Thermal
786 regime of the San Andreas fault near Parkield, California, *J. Geophys. Res.*, *102*, 27,575–
787 27,585, 1997.

788 Savage, M. K., Lower crustal anisotropy or dipping boundaries? Effects on receiver func-
789 tions and a case study in New Zealand, *J. Geophys. Res.*, *103*, 15,069–15,087, 1998.

Schwartz, S. Y., and J. M. Rokosky, Slow slip events and seismic tremor at circum-Pacific subduction zones, *Rev. Geophys.*, *45*, RG3004, doi:10.1029/2006RG000,208., 2007.

Shapiro, N. M., M. Campillo, L. Stehly, and M. H. Ritzwoller, High-resolution surface-wave tomography from ambient seismic noise, *Science*, *307*, 1615–1618, 2005.

Shelly, D. R., and J. L. Hardebeck, Precise tremor source location and amplitude variations along the lower-crustal central San Andreas Fault, *Geophys. Res. Lett.*, *37*, L14,301, 2010.

Shiomi, K., and J. Park, Structural features of the subducting slab beneath the Kii Peninsula, central Japan: Seismic evidence of slab segmentation, dehydration and anisotropy, *J. Geophys. Res.*, *113*, B10,318, doi:10.1029/2007JB005,535, 2008.

Thomas, A. M., R. N. Nadeau, and R. Burgmann, Tremor-tide correlations and near-lithostatic pore pressure on the deep san andreas fault, *Nature*, *462*, 1048–1051, 2009.

Thomson, C. J., The 'gap' between seismic ray theory and 'full' wavefield extrapolation, *Geophys. J. Int.*, *137*, 364–380, 1999.

Thurber, C. H., S. Roecker, K. Roberts, M. Gold, L. Powell, and K. Rittger, Earthquake locations and three-dimensional fault zone structure along the creeping section of the San Andreas fault near Parkfield, CA: Preparing for SAFOD, *Geophys. Res. Lett.*, *30*, 1112, 2003.

Thurber, C. H., H. Zhang, T. M. Brocher, and V. Langenheim, Regional three-dimensional seismic velocity model of the crust and uppermost mantle of northern California, *J. Geophys. Res.*, *114*, B01,304, doi:10.1029/2008JB005,766, 2009.

Titus, S. J., C. DeMets, and B. Tikoff, Thirty-five-year creep rates for the creeping segment of the San Andreas fault and the effects of the 2004 Parkfield earthquake: Con-

straints from alignment arrays, continuous global positioning system, and creepmeters, *Bull. Seism. Soc. Am.*, *96*, S250–S268, 2006.

Townend, J., and M. D. Zoback, Regional tectonic stress near the San Andreas Fault in central and southern California, *Geophys. Res. Lett.*, *31*, L15S11, 2004.

Trehu, A. M., and W. H. Wheeler, Possible evidence for subducted sedimentary materials beneath Central California, *Geology*, *15*, 254–258, 1987.

Waldhauser, F., Near-real-time double-difference event location using long-term seismic archives, with application to northern California, *Bull. Seism. Soc. Am.*, *99*, 2736–2748, 2009.

Walter, A. W., and W. D. Mooney, Crustal structure of the Diablo and Gabilan Ranges, Central California - A reinterpretation of existing data, *Bull. Seism. Soc. Am.*, *72*, 1567–1590, 1982.

Ward, D., K. Mahan, and V. Schulte-Pelkum, Roles of quartz and mica in seismic anisotropy of mylonites, *Geophys. J. Int.*, *190*, 123–1134, 2012.

Watanabe, T., Y. Shirasugi, H. Yano, and K. Michibayashi, Seismic velocity in antigorite-bearing serpentinite mylonites, in *Deformation Mechanisms, Rheology and Tectonics: Microstructures, Mechanics and Anisotropy*, vol. 360, edited by D. J. Prior, E. H. Rutter, and D. J. Tatham, pp. 97–112, Geological Society, London, Special Publications, 2011.

Wilson, C. K., C. H. Jones, P. Molnar, A. F. Sheehan, and O. S. Boyd, Distributed deformation in the lower crust and upper mantle beneath a continental strike-slip fault zone: Marlborough fault system, South Island, New Zealand, *Geology*, *32*, 837–840, 2004.

Yan, Z., and R. W. Clayton, Regional mapping of the crustal structure in southern California from receiver functions, *J. Geophys. Res.*, *112*, B05,311, doi:10.1029/2006JB004,622, 2007.

Zeng, X., C. H. Thurber, D. R. Shelly, N. Bennington, E. Cochran, and R. Harrington, 3D P and S wave velocity structure and tremor location in the Parkfield region, in *Fall Meeting*, American Geophysical Union, 2014.

Zhang, H., Y. Liu, C. Thurber, and S. Roecker, Three-dimensional shear-wave splitting tomography in the Parkfield, California, region, *Geophys. Res. Lett.*, *34*, L24,308, 2007a.

Zhang, X., H. Paulssen, S. Lebedev, and T. Meier, Surface wave tomography of the Gulf of California, *Geophys. Res. Lett.*, *34*, L15,305, doi:10.1029/2007GL030,631, 2007b.

Zhu, L., Crustal structure across the San Andreas Fault, southern California from teleseismic converted waves, *Earth Planet. Sci. Lett.*, *79*, 183–190, 2000.

Zhu, L., and H. Kanamori, Moho depth variation in southern California from teleseismic receiver functions, *J. Geophys. Res.*, *105*, 2969–2980, 2000.

Zoback, M. D., M. L. Zoback, J. P. Eaton, V. S. Mount, and J. Suppe, New evidence on the state of stress of the San Andreas Fault, *Science*, *238*, 1105–1111, 1987.

Table 1. Results of estimated parameters (in bold face) for the layered anisotropic crustal models. Uncertainty is shown in parantheses. In model 1 the total crustal thickness is >25 km. The trend of the slow axis is the best determined parameters. In model 2 the total crustal thickness is 20 km, however these estimates have large uncertainties and are highly non-unique.

Model 1: Upper crustal layer

Thickness (km)	Density (kg m^{-3})	V_P (km s^{-1})	V_S (km s^{-1})	% aniso	Trend (°)	Plunge (°)
2.5 (0.2)	2700	6.4	3.6	**-58 (4.0)**	**45 (7)**	**48 (4)**
25	2700	6.4	3.6	-	-	-
0	3300	7.8	4.5	-	-	-

Model 2: Layered crustal anisotropy

Thickness (km)	Density (kg m^{-3})	V_P (km s^{-1})	V_S (km s^{-1})	% aniso	Trend (°)	Plunge (°)
3.9 (1.8)	2700	6.4	3.6	**-46 (29)**	**45 (42)**	**49 (21)**
8.8 (2.9)	2700	6.4	3.6	**-28 (22)**	**222 (52)**	**52 (22)**
10.0	2700	6.4	3.6	-	-	-
0	3300	7.8	4.5	-	-	-

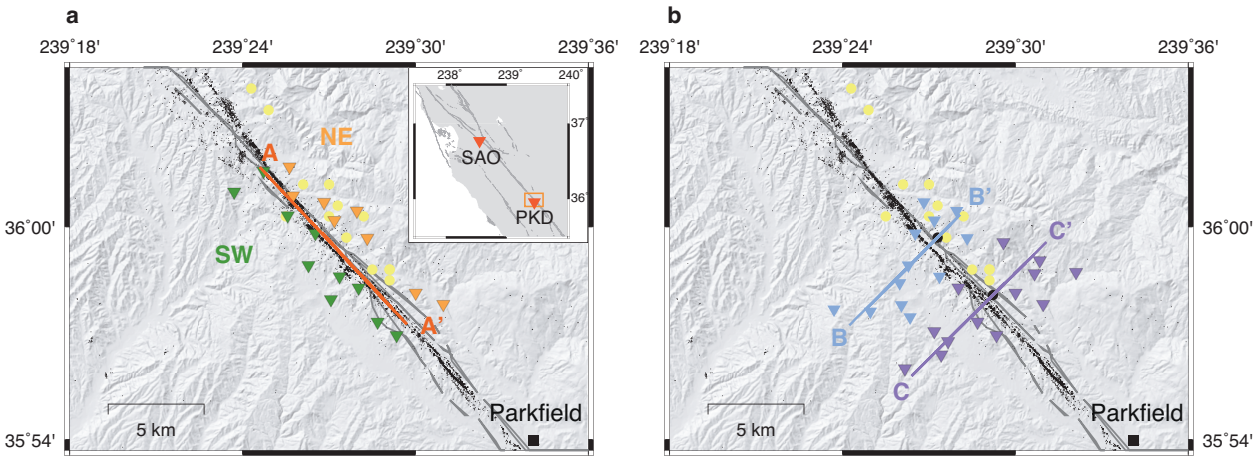

Figure 1. Location of broadband seismograph stations of the PASO network near Parkfield, California, shown by the inverted triangles. The inset shows the location of stations SAO and PKD relative to the area in (a) and (b) shown as an orange-colored box. In (a) the stations located within 2 km of the line A-A' that roughly follows the trace of the San Andreas Fault (SAF, shown as gray lines) are separated into 2 subsets, depending on their location with respect to the line A-A'. In (b) the stations are separated into 2 subsets along profiles B-B' and C-C' that straddle the SAF. Black dots are regular earthquakes from *Waldhauser* [2009]. Yellow circles are low-frequency earthquakes from *Shelly and Hardebeck* [2010].

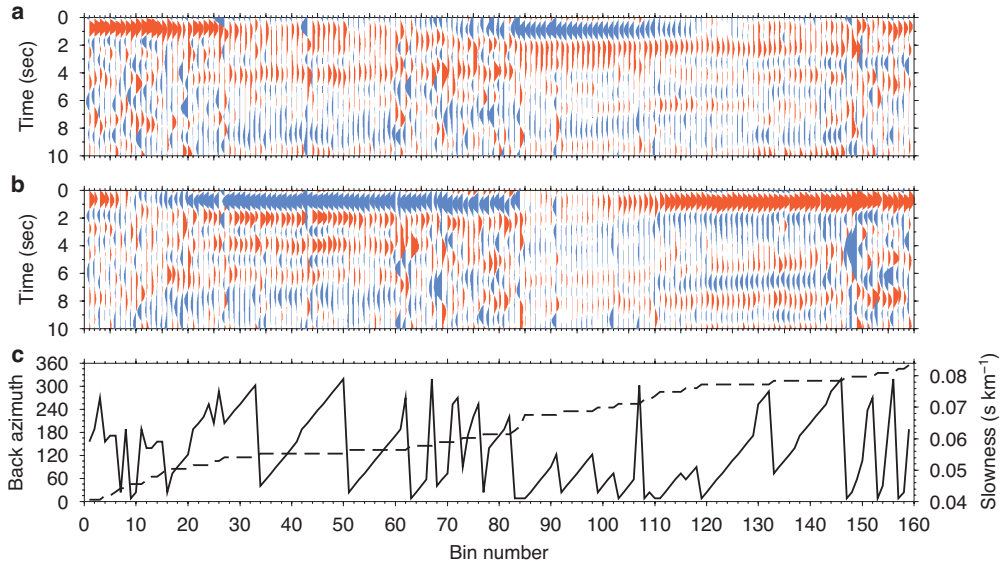

Figure 2. Radial (a) and transverse (b) component receiver function data for station SAO. Panel (c) shows the back-azimuth (dashed line) and slowness (solid line) distribution of teleseismic events. These data are dominated by an early (∼1-2 sec) pulse with strong back-azimuth variations in both radial and transverse components.

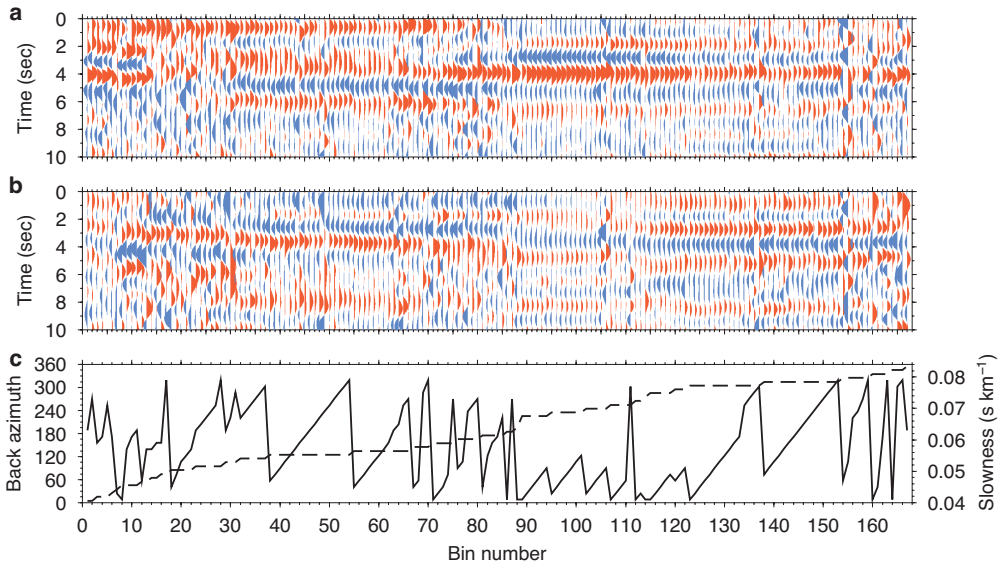

Figure 3. Radial (a) and transverse (b) component receiver function data for station PKD. Figure format is the same as Figure (2). These data show complex patterns in both radial and transverse components.

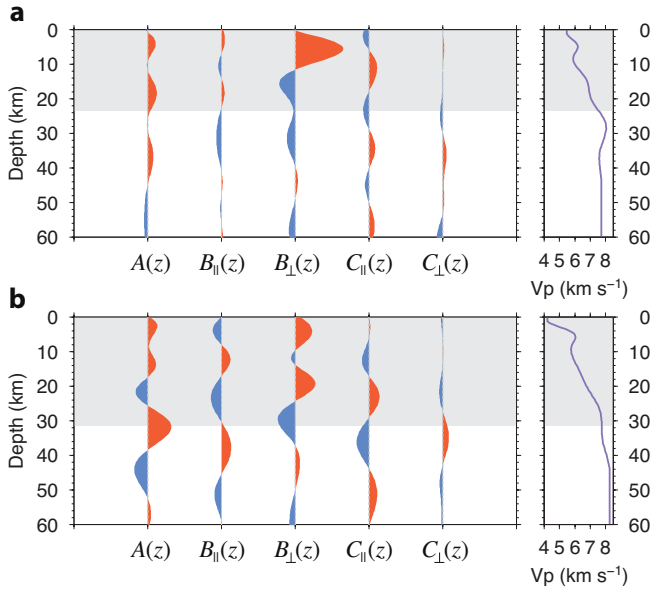

Figure 4. Harmonic decomposition of receiver functions for stations SAO (a) and PKD (b). Each vertical trace corresponds with a given harmonic, identified on the horizontal axis. The shaded area corresponds to the depth over which the inversion for α_C is carried out. The right panel shows the velocity model extracted from *Lin et al.* [2010], used to migrate receiver functions to depth.

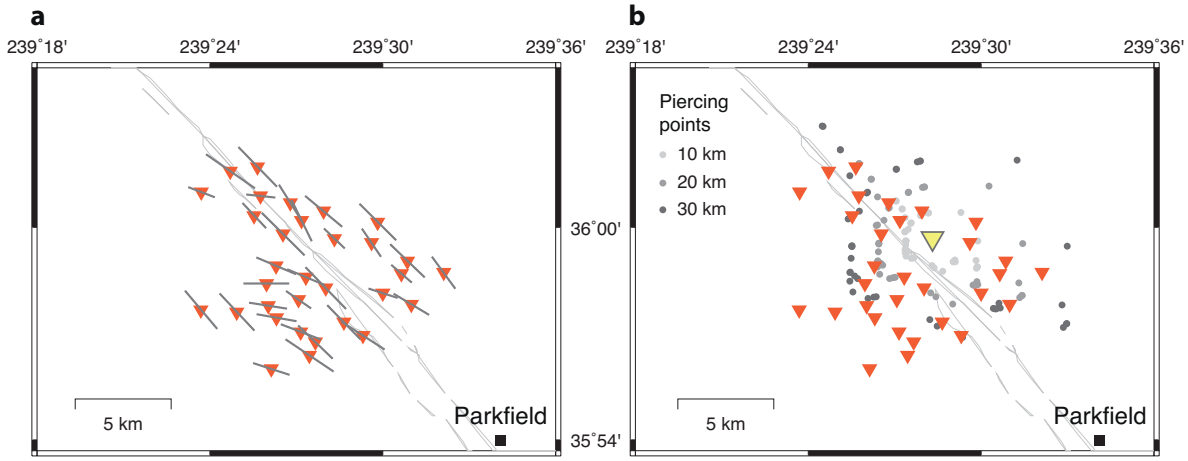

Figure 5. (a) Results of estimated α_C at each station, calculated from the surface to Moho depth (average of 35 km), shown as gray bars. These vectors point either in the direction of strike for dipping faults, or in the direction of (or perpendicular to) the fast (slow) axis of seismic anisotropy. These azimuths are generally parallel to the main strike of the SAF over an area of $\sim$100 km^2, indicating uniform orientation of fabric or structures around the SAF. (b) Piercing points at virtual interfaces of 10, 20 and 30 km for station CVCR (yellow triangle), shown as grey dots.

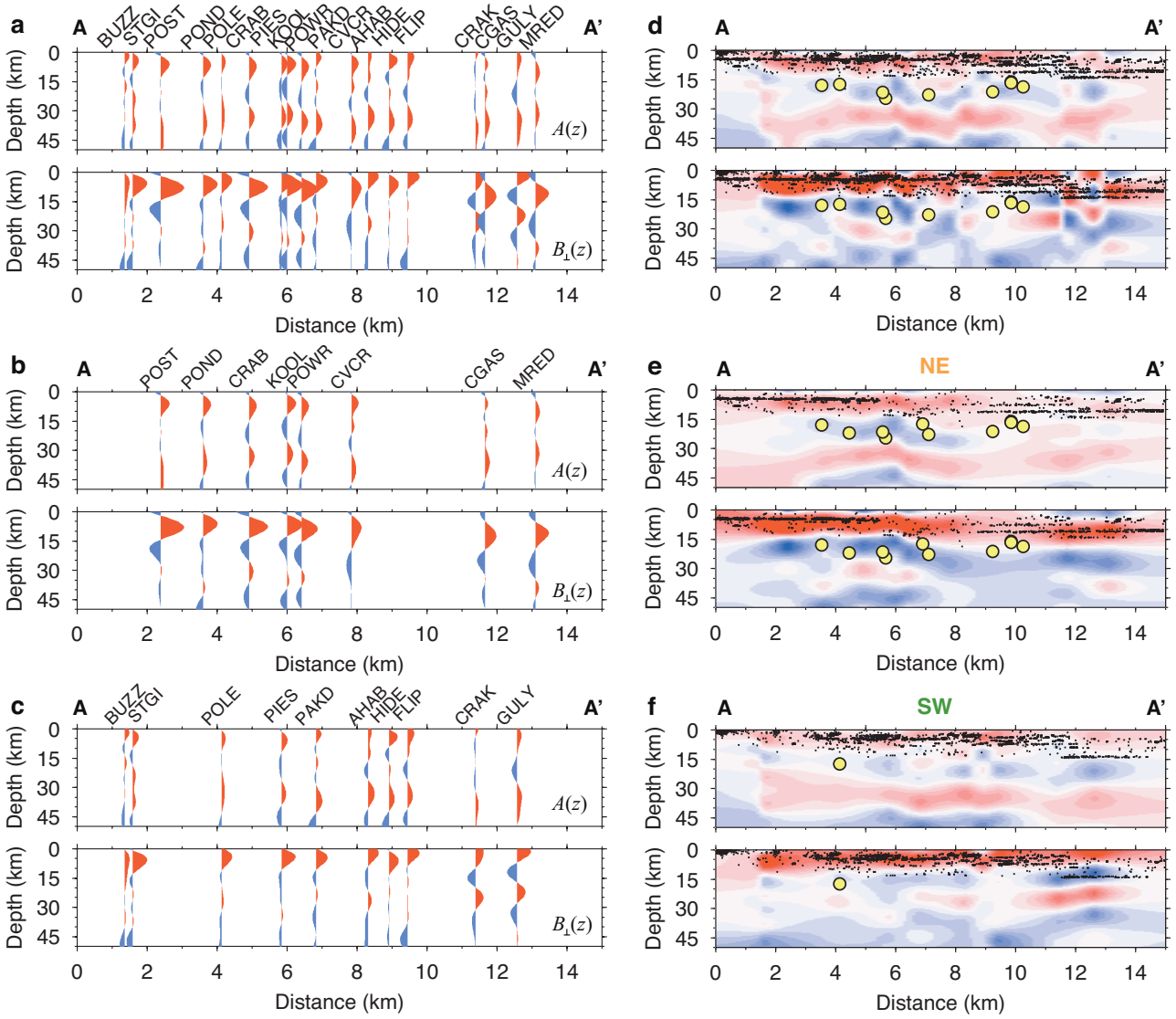

Figure 6. (a-c) Results of harmonic decomposition showing the A and $B_\perp$ components along the profile A-A' in Figure (1a). (d-f) Interpolated image of the A and $B_\perp$ terms at each depth increment. Panels (a) and (d) show results for all stations along A-A', whereas panels (b,c) and (e,f) show the same results for the two station subsets located to the northeast (b,e) or to the southwest (c,f) of line A-A' (Fig. 1). Black dots are regular earthquakes from *Waldhauser* [2009]. Yellow circles are low-frequency earthquakes from *Shelly and Hardebeck* [2010].

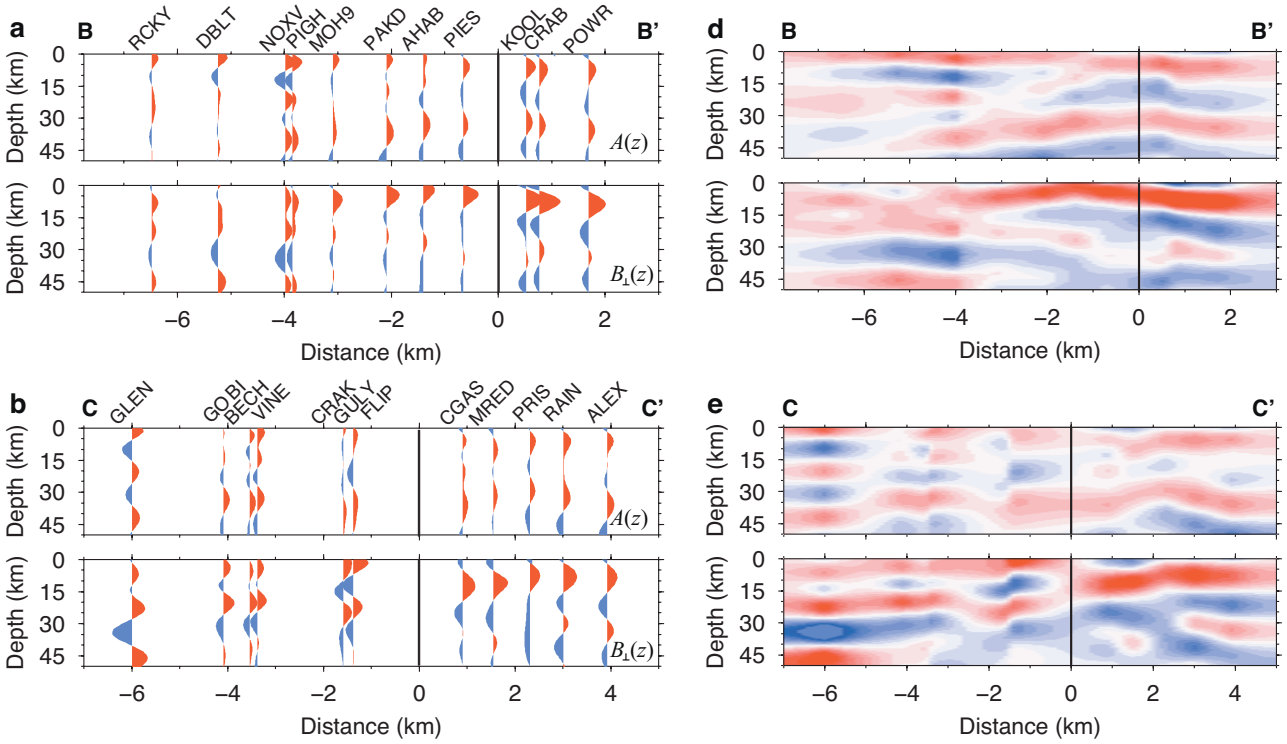

Figure 7. Results of harmonic decomposition for stations located along two profiles that straddle the SAF (Fig. 1b). Figure format is the same as Figure (6).

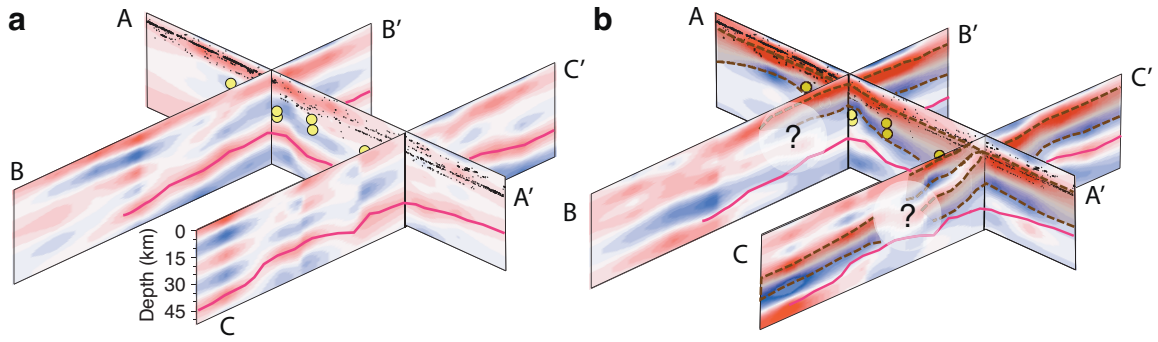

Figure 8. Pseudo-3-D rendering of the (a) isotropic and (b) anisotropic component profiles around the San Andreas Fault. The strike-parallel profile (A-A') corresponds to the NE side of the fault. The purple line indicates the interpreted Moho horizon. Dark shaded area with brown dashed lines in (b) shows the extent of the mid-crustal anisotropic layer. Question marks outline regions where the structural continuity is ambiguous. Horizontal scale is stretched ∼15 times.

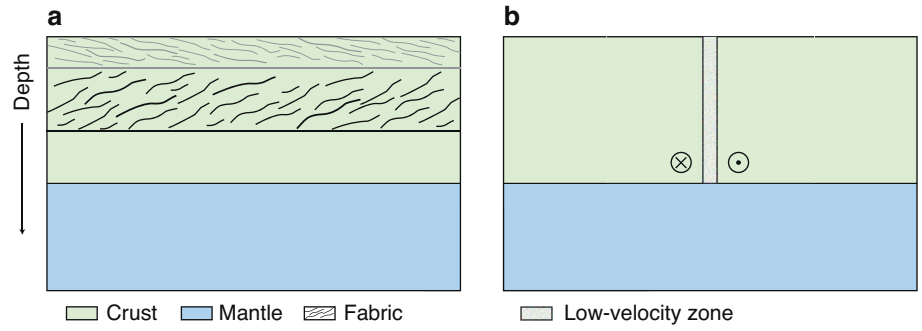

Figure 9. End-member crustal models used to explain receiver function data around Parkfield. The first model (a) represents a crust with upper and mid crustal anisotropy. Model (b) represents a vertical low-velocity fault zone penetrating the entire crust. Both models are underlain by an isotropic mantle half-space.

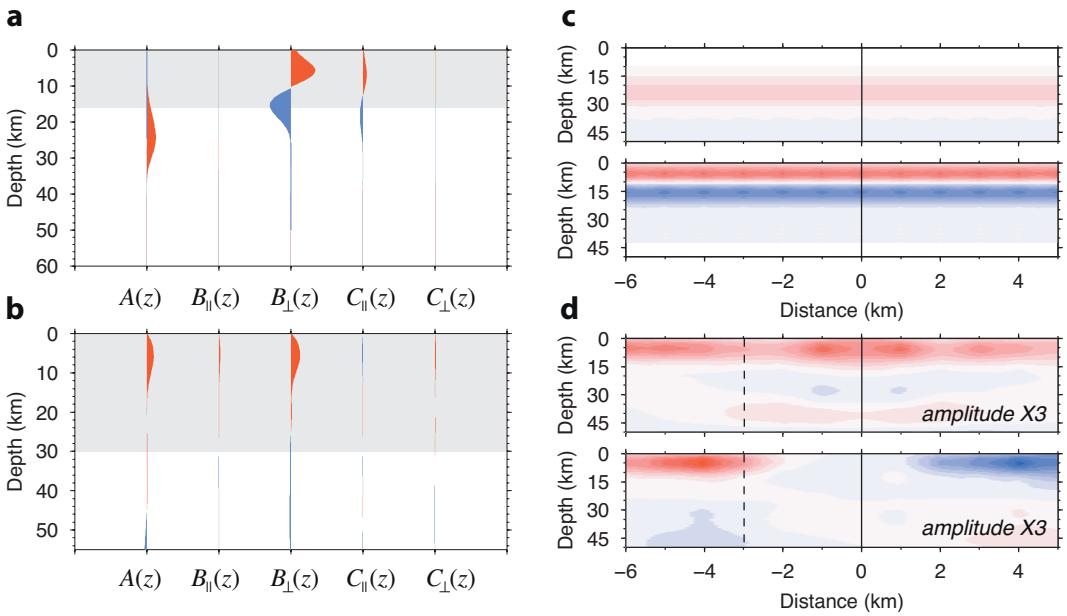

Figure 10. Harmonic decomposition of synthetic receiver functions for the two crustal models (a,b). Results correspond to the bi-layered (upper and mid-crustal anisotropy) model (a) and the vertical low-velocity zone model (b), respectively. (c) and (d) show interpolated images of the A and $B_\perp$ terms for profiles straddling a virtual fault, for a uniformly anisotropic lower crust (c) and for a vertically-dipping low-velocity zone (d). Amplitudes in (d) are scaled up three times. The vertical solid and dashed lines in (c) and (d) show the location of the San Adreas Fault and that of station SAO along the profile, respectively.

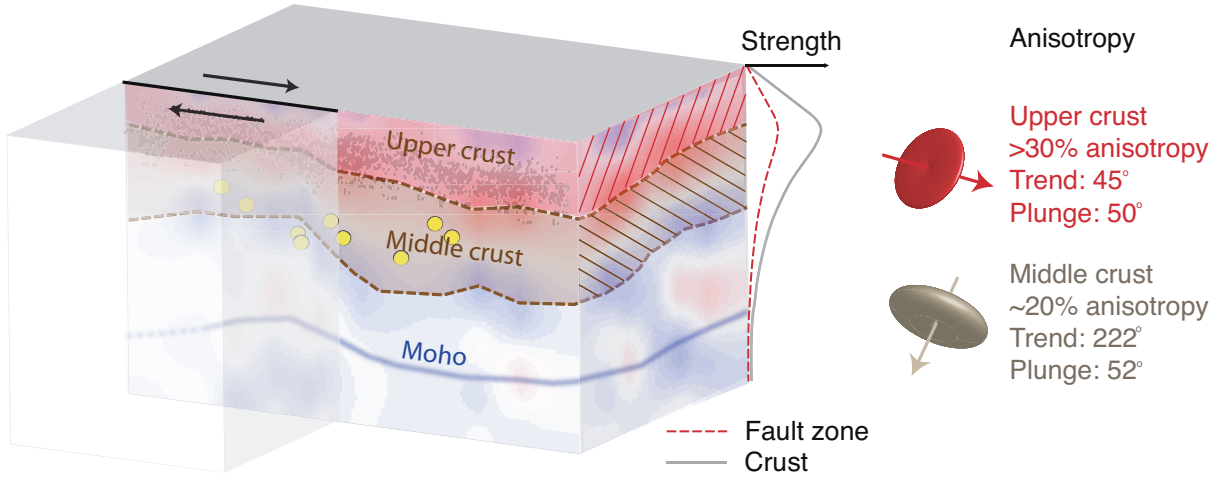

Figure 11. Interpretation of receiver function results. The soft-colored sides on the NE block show the anisotropic component (profiles A-A' and half of C-C') as in Figure (8b). The hachured patterns represent the orientation of weak planar fabric in the upper and middle crust. The estimated anisotropy is shown on the right, where the disk shapes represent the orientation of the weak fabric, given in terms of the weak axis direction (arrows and values on the right). The idealized strength profiles represent the inferred weakening of the fault zone caused by crustal fabric, due to the combined effects of elevated pore-fluid pressure in the upper brittle crust and weak anisotropic minerals.